Supplementary Materials

Wake-sleep cycles are severely disrupted by diseases affecting cytoplasmic homeostasis

Authors: Stephen Beesley[1,†], Dae Wook Kim[2,†], Matthew D'Alessandro[1,‡] ,Yuanhu Jin[1], Kwangjun Lee[1], Hyunjeong Joo[1,3], Young Yang[3], Robert J. Tomko Jr[1], John Faulkner[4], Joshua Gamsby[4], Jae Kyoung Kim[2,*], Choogon Lee[1,*]

Correspondence: Choogon.lee@med.fsu.edu and jaekkim@kaist.ac.kr

This PDF file includes:

Materials and Methods

Supplemental figures:

Other Supplementary Materials for this manuscript include the following:

Movie S1. Real time monitoring of PER2-Venus trafficking in U2OS cells.

Materials and methods

Genotyping: PCR Primers

Atg5^{Flox} and wt alleles:

Fwd: 5'gaatatgaaggcacacccctgaaatg3'
Rev: 5'gtactgcataatggtttaactcttgc3'
neo casset fwd: 5'acaacgtcgagcacagctgcgcaagg3'

Amplicon: wt ~357 bp; floxed ~700 bp

P62-/- and wt alleles:

p62 geno_1: 5'CTGCATGTCTTCTCCCATGAC3'
p62 geno_2: 5'TAGATACCTAGGTGAGCTCTG3'
p62 geno_3: 5'CTTACGGGTCCTTTTCCCAAC3'
p62 geno_4: 5'TCCTCCTTGCCCAGAAGATAG3'

Amplicon: ~wt 300 bp; ko ~600 bp

CAG-cre-ER:
FW: 5'ccagcaacatttgggcca3'
Rev: 5'cccaccgtcagtacgtgaga3'

Amplicon: ~wt no band; tg ~260 bp

Per2^{Luc}

Fw: 5'ctgtgtttactgcgagagt3'
Rev: 5'gggtccatgtgattagaaac3'
Luciferase rev:5'taaaaccgggaggtagatgaga3'

Amplicon: ~wt 230 bp; KI ~680 bp

Analysis of circadian behavioral rhythms

All mice were individually housed in wheel-running cages, with free access to food and water except the mice described in Fig 1D. Wheel running activity was recorded and analyzed using ClockLab (Actimetrics, Wilmette, IL). Since it is not possible to calculate long-term periods and statistical values due to unstable phase angle in all individual *Atg5* and *P62* mutant mice, short-term periods were calculated over a short duration where phase angle is stable (1-2 weeks) in individual mutant mice. Free-running period was calculated using a Chi-square periodogram with six-minute resolution between hours 10 and 36 (ClockLab). In Fig. 1C and fig. S4, all animals were initially placed in a 12h light:12h dark (LD) cycle, for at least 7 days. Mice were then transferred to constant darkness (DD), for approximately two weeks, to measure baseline activity. *Atg5* deletion was induced in the whole body in *Atg5*$^{fl/+}$ *or Atg5*$^{fl/fl}$*/CAG-CreEsr-1* mutant mice by feeding them tamoxifen-containing chow (Harlan TD.130859; 0.4g tamoxifen/kg food) for two weeks. The wt control received the same treatment. We showed that this tamoxifen treatment does not induce circadian disruption in wt and floxed mutant mice without the cre transgene (1).

After two weeks, any remaining tamoxifen chow was removed and replaced with regular mouse chow for the remainder of the recordings. In Fig. 1E, C57BL/6J mice were entrained in LD cycles followed by DD for 2 weeks, showing the baseline activity. A hypocalorie diet (2/3 of daily consumption) was given at ZT12 of the previous LD cycle for 12 days (indicated by the green line) before returning to ad libitum. The red line indicates continuous activity onset if the mice had not been subjected to starvation. The circadian period before starvation and from the last 7 days during starvation was calculated and compared by paired t-test.

For Fig 6A, Locomotor, period and activity levels of Tg4510 and non-transgenic litter mate controls were calculated as previously described (2). Briefly, 3-month-old male and female mice (n=8 each) were individually housed with *ad libitum* access to food and water in a 12:12 light/dark cycle (LD). Mice were then moved to running wheel cages (Lafayette Instrument, Lafayette, IN) in light-tight, sound-attenuated cabinets and entrained to a 12:12 LD cycle for ~9 days. To assess free-running period, mice were then exposed to constant darkness (DD) for ~14 days. Activity data was recorded in 5 min bins using Scurry Activity Monitoring Software (Lafayette Instrument, Lafayette, IN). Period and activity levels were calculated using Clocklab (Version 6; Actimetrics, Wilmette, IL).

Antibodies

Antibodies to clock proteins were generated against recombinant clock proteins expressed and have been previously reported (3-5). PER1-GP62, PER2-GP58, human PER2-GP49 (U2OS), BM1-2-GP, C1-GP (CRY1), CK1δ-GP and CK1ε-GP antibodies were used at 1:1,000 dilution in 5% milk–Tris-buffered saline containing 0.05% Tween 20 solution. PER1-GP62 and human PER2-GP49 antibodies were used for immunoblots of U2OS samples and ICC in Fig S10. These antibodies have been validated using knockout tissue samples. Rabbit anti-ACTIN antibody (Sigma, A5060) was used at 1:2,000. Anti-LC3 and P62 antibodies were from Cell Signaling (#12741) and Abcam (#56416), respectively.

Adenoviral vectors and plasmids

The inducible *Per2-Venus* transgene was generated by knocking in the Venus sequence between the last amino acid codon and stop codon in the previously described inducible tetO-Per2; CMV-rtTA-pAdTrack plasmid (6). The Track vector was subsequently cut with PmeI for linearization and then transformed into the *E.coli* BJ5183 strain, together with the pAdEasy adenoviral backbone vector, to generate a complete adenoviral vector through *in vivo* recombination. Generation and purification of the recombinant adenovirus was also performed as described previously (7). Titers of the purified virus to achieve >95% infection efficiency were determined by counting green fluorescent protein (GFP)-expressing cells, in culture plates, infected with different concentrations of adenoviruses (8). In Fig. 2 and movie S1, induction of PER2-Venus was stopped for 12 hrs by replacing doxycycline DMEM (2 ug/ul dox) with fresh DMEM before the images and movies were taken. For Fig 2H, U2OS cells were further treated with control 100% DMEM, 5% AA medium or 5% AA + 2mM 3-MA for another 12 hrs before the images were taken. For Fig 2I, the cells were further monitored for 27 hrs under the normal medium 100% DMEM. For Fig 2K, the inducible Per2-Venus Track plasmid and a *CMV-mCerulean3-LaminB1* plasmid were cotransfected into U2OS cells which then were subjected to 5% AA medium for 12 hrs to demonstrate that the Per2-Venus ring is outside the nucleus. For Fig S5C, the inducible Per2-Venus Track plasmid and pcDNA-CK1δ were cotransfected into U2OS cells. The images were taken 12 hrs later after induction had been discontinued. 200 ng Per2-Venus plasmid and 500 ng CK1δ plasmid were used. For Adenoviruses expressing *Per2* promoter-*Per2* cDNA (*Per2-cPer2*), *Per2* promoter-luciferase reporter (*Per2-luc*) and *CMV-Egfp* (control) used

in Fig. 5F were described previously (8). For Fig. 5F, *Egfp* adenovirus was co-infected with *Per2-Luc* adenovirus in control and adipocyte samples whereas, in rescued samples, *Per2-cPer2* adenovirus was co-infected with *Per2-Luc* adenovirus. *pcDNA-Per1*, *Per2* and *CK1δ* and *CK1ε* plasmids were described previously (8).

Transfection, Immunoblotting and Immunocytochemistry

Per1, *Per2*, *CK1δ* plasmids were transfected into HEK293a cells using Qiagen's PolyFect Transfection Reagent. Briefly, the PolyFect reagent was mixed with 1μg plasmid DNA and combined with 150μL of DMEM. The solution was mixed briefly and incubated at room temperature for 10 minutes. The mixture was added to the cell medium and incubated for 48 hours before harvest. For Fig 4F, 300 ng *Per1* and 50 ng *CK1δ* were used for transfection. If *CK1δ* is used more than 500 ng, the mutant PER1 can be also hyperphosphorylated to some level probably due to random interaction instead of the stoichiometric interaction.

The cells in 6 cm dishes were harvested and flash-frozen on dry ice. Protein extraction and immunoblotting were performed as previously described (6). Briefly, tissues or cells were homogenized at 4°C in 10 volumes of extraction buffer (EB) (0.4M NaCl, 20mM HEPES (pH 7.5), 1mM EDTA, 5mM NaF, 1 mM dithiothreitol, 0.3% Triton X-100, 5% glycerol, 0.25mM phenylmethylsulfonyl fluoride, 10mg of aprotinin per ml, 5mg of leupeptin per ml, 1mg of pepstatin A per ml). Homogenates were cleared by centrifugation for 12 min, 12,000g at 4°C. Supernatants were mixed with 2x sample buffer and boiled. Proteins were separated by electrophoresis through SDS polyacrylamide gels and then transferred to nitrocellulose membranes. Membranes were blocked with 5% non-fat dry milk in Tris-buffered saline containing 0.05% Tween-20, incubated with primary antibodies overnight followed by incubation with secondary antibodies for 1 hr. The blots were developed using an enhanced chemiluminescence substrate (WestFemto, ThermoFisher Scientific).

Tissue collection and western blot analysis of pTau levels were performed as previously described (9). Briefly, after the evaluation of free-running period in DD, mice were euthanized by cervical dislocation and rapid decapitation, brains were harvested, and the hypothalamus was dissected before being flash frozen for further processing. Hypothalamic tissue was lysed in M-PER with phosphatase and protease inhibitors using sonication. Protein concentrations were determined using a BCA assay kit (Thermo Scientific). Equal amounts of protein from brain lysate (30 μg) were resolved using 9.5% Tris-glycine polyacrylamide gels under reducing conditions. Proteins were transferred to nitrocellulose membranes (Bio-rad, Hercules CA), and blocked for 1 h at room temperature in blocking buffer which was a 5% non-fat milk (Labscientific, Inc., Livingston, NJ) and tris-buffered saline containing 0.1% Tween-20 solution (Boston Bioproducts, Ashland, MA). Membranes were then incubated overnight at 4 °C with either anti-phospho-tau ($pSer^{396}$) at 1:1000, (Anaspec, Fremont, CA) or anti-B-Actin at 1:7500 (Sigma-Aldrich, St Louis, MO), washed 3 × 10 min in tris-buffered saline with 0.1% Tween-20 (TBS-T) then placed in blocking buffer combined with HRP-conjugated secondary antibody diluted 1:7500 and left to incubate at room temperature for 1 h. After thorough washing with TBS-T, bands were visualized using enhanced chemiluminescence (ECL; Thermo scientific) with an image analyzer (Amersham imager 600).

For ICC, U2OS cells were plated on glass cover slips in six-well plates and grown to 50% confluency. The cells were treated with 50% horse serum and fixed 36 hrs later with 4% paraformaldehyde (PFA) in 1X PBS for ten minutes on a shaker at room temperature. The PFA

was then washed off with 1X PBS three times for five minutes per wash. The cells were then blocked in 5% fetal bovine serum (FBS) supplemented with 0.5% TritonX-100 in PBS for 30 minutes at room temperature. The cells were incubated in 1:300 dilutions of PER1-GP62 or human PER2-GP49 antibody overnight, at 4°C, on a shaker. The following day, the primary antibodies were removed, and the cells were washed in 1x PBS 3 times for 5 minutes per wash. A Texas Red-conjugated, goat anti-guinea pig IgG (H+L) secondary antibody (Thermo Scientific #PA1-28595) was added to the samples, at 1:300 concentration, for two hours at room temperature with shaking. The secondary antibody was removed and cells were washed with 1X PBS 3 times for 5 minutes per wash. Vectashield antifade (Vector Labs) mounting medium with DAPI (H-1200) was added to the coverslips. The coverslips were placed on microscope slides, and the edges were sealed. The images were obtained using a fluorescent microscope.

Mathematical modeling

Development of the spatial stochastic model of the circadian clock

We extended the previous mathematical model of the mammalian circadian clock (10-14) to generate the spatial stochastic model (Fig. 3A) by using the agent-based modelling approach (15). Agent-based model is a class of computational models for simulating the actions of autonomous cellular components, which are called agents. Our model consists of four agents: *Per* mRNA, hypophosphorylated PER, hyperphosphorylated PER, and obstacles to PER trafficking. The agents follow specific rules about how they act and move (see Table 1 for details). In the model, *Per* mRNA is transcribed in the nucleus and then randomly moves. When *Per* mRNA reaches the cytoplasm, it is translated to PER protein. Then, PER protein transits toward the perinucleus by cytoplasmic flux and accumulates there (Fig 3A, (i)); this movement can be disrupted by the obstacles (Fig. 3A, (ii)). If the accumulated PER is hyperphosphorylated (Fig. 3A (iii)), it is translocated into the nucleus and inhibits its own transcriptional activator (Fig. 3A (iv)). See below for a detailed description of how the biochemical activity and the mobility of agents were simulated.

Simulation

All the simulations were performed using an open-source agent-based modelling software, NetLogo 6.0.4 (Center for Connected Learning and Computer-Based Modeling, Northwestern University, Evanston, IL) (16) and MATHEMATICA 11.0 (Wolfram Research Champaign, IL) with an Intel® Core™ i7-6700CPU 3.40 GHz computer hardware.

Size of cell, nucleus and agents in the model

For simplicity, we modelled the cell two-dimensionally, as a circle with unitless radius of d (fig. S10A). Then, the radius of nucleus was defined as $d/3$ so that the nucleus occupies about 10% of the cell area, consistent with the experimental data (17). The perinucleus (Fig. 3A, pink region and fig. S7A and B, red region) was defined as the annulus region around the nucleus whose area occupies about 15% of the cytoplasmic area. The inner periphery of the cytoplasm fig. S7A and B, green region) was defined as the annulus region around the perinuclear region whose area occupies about 20% of the cytoplasmic area. Each cytoplasmic obstacle was defined as a small circle with radius of $d/50$. Each PER molecule was modelled as a circle with radius of $d/100$, which facilitates modelling of their nuclear import and export (see Mobility of agent section below and fig. S10B-F for details).

Simulation of biochemical reactions

The biochemical reactions of an individual agent were simulated with a Markov chain scheme (18, 19). If an individual agent x is involved in N reactions (i=1,….N), then the number that the

*i*th reaction involving x occurs during $[t, t+\Delta t]$, $N_i^x(t)$, follows a Poisson distribution: $N_i^x(t) \sim Pois(p_i^x(t))$, where $p_i^x(t)$ is the probability that the *i*th reaction involving x occurs during $[t, t+\Delta t]$ (20-22). Thus, the probability that at least one reaction involving x occurs during $[t, t+\Delta t]$ becomes $1 - exp(\sum_{i=1}^{N} p_i^x(t))$ (20-22), which determines whether at least one reaction involving x occurs for $[t, t+\Delta t]$ or not. Δt was chosen small enough so that the probability that the multiple reactions involving x occur for $[t, t+\Delta t]$ could be neglected (23, 24). Thus, we assumed that each individual agent engages in at most one reaction for $[t, t+\Delta t]$.

Step 1. Decide whether an individual agent engages in a biochemical reaction or not for $[t, t+\Delta t]$.

1) Calculate the probability that a reaction involving x occurs for $[t, t+\Delta t]$: $1 - exp\left(\sum_{i=1}^{N} p_i^x(t)\right)$.

2) Get a uniform random number $u \in [0,1]$.

3) If $u \leq 1 - exp\left(\sum_{i=1}^{N} p_i^x(t)\right)$, a reaction involving x occurs for $[t, t+\Delta t]$. Otherwise, x does not.

Step 2. If a reaction involving x occurs, decide which reaction occurs for $[t, t+\Delta t]$.

1) Calculate the cumulative function $R_j(t) = \sum_{i=1}^{j} p_i^x(t)$ for $j = 1, \dots N$.

2) Get a uniform random number $v \in [0,1]$.

3) Identify the reaction to carry out for x by finding the i for which $\frac{R_{i-1}(t)}{R_N(t)} < v \leq \frac{R_i(t)}{R_N(t)}$

4) Change the state of x by carrying out the *i*th reaction.

By repeating this scheme for all agents, the state of agents is updated.

The probability that each reaction occurs for Δt was obtained by adjusting the parameter values of the previous mathematical model of the mammalian circadian clock (10-13) (Table 2). The hyperphosphorylated PER is set to be more likely degraded than the hypophosphorylated PER (10, 25-27). In Fig. 4C and D, the probability that *Per* mRNA is transcribed for Δt was doubled to capture the strong *Per* mRNA rhythmicity even in absence of the bistability in PER hyperphosphorylation. In Fig 5E, the probability that *Per* mRNA is transcribed for Δt was increased by 50% to restore the PER rhythmicity in the adipocytes.

Per mRNA transcription and the multisite phosphorylation of PER protein involve fast binding and unbinding reactions, which dramatically increases computation cost. Thus, we eliminated fast reactions and derived reaction probabilities for slow reactions by using a total quasi-steady state approximation (tQSSA) (28, 29) as described below. This dramatically reduces the computation cost but accurately approximates the original stochastic simulation (12, 30-32).

Modelling of Per mRNA transcription and PER protein translation

In the model, the transcription of *Per* mRNA is proportional to the number of free activators not sequestered by PER protein. To calculate the number of free activators at each time, we first derived the quasi-steady state of fraction of free activator, $f(P, A, K_d)$, by using tQSSA under the assumption of fast binding and unbinding between PER protein and the activator (10-14):

$$f(P, A, K_d) = \frac{A - P - K_d + \sqrt{(A - P - K_d)^2 + 4 \cdot A \cdot K_d}}{2A}$$

where P, A and K_d denote the nuclear concentration of PER protein, that of activator and the dissociation constant between them.

$f(P, A, K_d)$ was obtained from a reaction-limited system where the reactions of agents are slower than their movement (i.e. ODE system) (33). Thus, to use $f(P, A, K_d)$ in our spatial model,

we divided the nucleus into small regions, $\mathcal{R}_i$ for $i = 1, \dots, 16$ (fig. S10A) and obtained the reaction-limited system:

$$\mathcal{R}_1 = \left\{(r,\theta)\middle| 0 \le r < \frac{r_n}{2},\ 0 \le \theta < \frac{\pi}{4}\right\}$$
$$\mathcal{R}_i = \left\{(r,\theta)\middle| 0 < r < \frac{r_n}{2},\ \frac{\pi}{4}\cdot(i-1) \le \theta < \frac{\pi}{4}\cdot i\right\} \text{ for } i = 2, \dots, 8$$
$$\mathcal{R}_j = \left\{(r,\theta)\middle| \frac{r_n}{2} \le r \le r_n,\ \frac{\pi}{4}\cdot(i-9) \le \theta < \frac{\pi}{4}\cdot(i-8)\right\} \text{ for } j = 9, \dots, 16$$

where r_n denotes the nuclear radius. Then, by multiplying the total number of activators in $\mathcal{R}_i$, $N^t_{\mathcal{R}_i}$, by $f\left(P_{\mathcal{R}_i}(t), A, K_d\right)$ where $P_{\mathcal{R}_i}(t)$ is the concentration of PER in $\mathcal{R}_i$ at t, the number of free activators in $\mathcal{R}_i$ at time t, $N^f_{\mathcal{R}_i}(t)$, was calculated (i.e. $N^f_{\mathcal{R}_i}(t) = N^t_{\mathcal{R}_i} f\left(P_{\mathcal{R}_i}(t), A, K_d\right)$). Note that as we assumed that a fixed number of activators are uniformly distributed in the nucleus, $N^t_{\mathcal{R}_i}$ is constant. Then, each of $N^f_{\mathcal{R}_i}(t)$ free activators can promote the *Per* transcription with the probability p_{a_1} at randomly chosen positions in $\mathcal{R}_i$ for $[t, t + \Delta t]$.

The transcribed mRNA is translated in the outside of the inner periphery of the cytoplasm (fig. S7A and B, blue region) as ribosomes are expected to be largely distributed there (34-36), and ribosomes near the nucleus are sequestered to the rough endoplasmic reticulum (37).

Modelling of the multisite phosphorylation of PER protein

We derived the reaction probabilities for hyperphosphorylation and dephosphorylation for Δt by using the tQSSA (28, 29). Specifically, the multisite phosphorylation (Fig. 3B) consists of reactions among PER, CK1δ/ε and PP1 as follows:

$$PER + CK1 \underset{d_1}{\overset{a_1}{\rightleftarrows}} PER{:}CK1 = C_1 \xrightarrow{k_1} PER_P + CK1$$
$$PER_P + CK1 \underset{d_2}{\overset{a_2}{\rightleftarrows}} PER_P{:}CK1 = C_2 \xrightarrow{k_2} PER_{PP} + CK1$$
$$PER_P + PP1 \underset{d_3}{\overset{a_3}{\rightleftarrows}} PER_P{:}PP1 = C_3 \xrightarrow{k_3} PER + PP1$$
$$PER_{PP} + PP1 \underset{d_4}{\overset{a_4}{\rightleftarrows}} PER_{PP}{:}PP1 = C_4 \xrightarrow{k_4} PER_P + PP1$$

where PER, PER_P, PER_{PP}, $CK1$ and $PP1$ are non-, prime- and hyperphosphorylated PER, CK1δ/ε and PP1, respectively, and C_i for $i = 1, 2, 3$ and 4 are the intermediate complexes.

These reactions can be described with the ODE system based on mass action kinetics:

$$\begin{aligned}
\frac{d[PER]}{dt} &= -a_1[PER]\cdot[CK1] + d_1[C_1] + k_3[C_3],\\
\frac{d[PER_p]}{dt} &= k_1[C_1] - a_2\left[PER_p\right]\cdot[CK1] + d_2[C_2] - a_3\left[PER_p\right]\cdot[PP1] + d_3[C_3] + k_4[C_4],\\
\frac{d[PER_{pp}]}{dt} &= k_2[C_2] - a_4\left[PER_{pp}\right]\cdot[PP1] + d_4[C_4],\\
\frac{d[C_1]}{dt} &= a_1[PER]\cdot[CK1] - (d_1 + k_1)[C_1],\\
\frac{d[C_2]}{dt} &= a_2\left[PER_p\right]\cdot[CK1] - (d_2 + k_2)[C_2], \qquad \cdots \text{(Eq. 1)}\\
\frac{d[C_3]}{dt} &= a_3[PER_p]\cdot[PP1] - (d_3 + k_3)[C_3],\\
\frac{d[C_4]}{dt} &= a_4[PER_{pp}]\cdot[PP1] - (d_4 + k_4)[C_4],\\
PER_{tot} &= [PER] + \left[PER_p\right] + \left[PER_{pp}\right] + [C_1] + [C_2] + [C_3] + [C_4],\\
CK1_{tot} &= [CK1] + [C_1] + [C_2],
\end{aligned}$$

$PP1_{tot} = [PP1] + [C_3] + [C_4]$.

The values of a_i, d_i and k_i for $i = 1, 2, 3$ and 4, were modified from (Table 3). In particular, $k_1 \ll k_2$ to capture the cooperativity in multisite PER phosphorylation (38). This cooperativity was eliminated in Fig. 4C and D (i.e. $k_1 = k_2$) to disrupt the bistability (Table 3). To reduce this system with tQSSA, we have replaced PER and PER_{pp} with slower variables $\overline{NP} \equiv PER + PER_p + C_1 + C_2 + C_3$ and $\overline{HP} \equiv PER_{pp} + C_4$, which represent the concentrations of hypo- and hyperphosphorylated PER, respectively. Compared to $\overline{NP}$ and $\overline{HP}$, which do not engage in fast binding and unbinding reactions (a_i and d_i), PER_p, C_1, C_2, C_3 and C_4 more rapidly reach their quasi-steady states (QSSs). These can be derived by solving $\frac{d[PER_p]}{dt} = 0$ and $\frac{d[C_i]}{dt} = 0$ for $i = 1, 2, 3$ and 4 in terms of $\overline{NP}$ and $\overline{HP}$. By substituting these QSSs, we can get the reduced system, which solely depends on $\overline{NP}$ and $\overline{HP}$:

$$\begin{aligned}
&\frac{d[\overline{NP}]}{dt} = -k_2 C_2([\overline{NP}], [\overline{HP}]) + k_4 C_4([\overline{NP}], [\overline{HP}]), \\
&\frac{d[\overline{HP}]}{dt} = k_2 C_2([\overline{NP}], [\overline{HP}]) - k_4 C_4([\overline{NP}], [\overline{HP}]), \qquad \cdots \text{(Eq. 2)} \\
&PER_{tot} = [\overline{NP}] + [\overline{HP}].
\end{aligned}$$

$k_2 C_2([\overline{NP}], [\overline{HP}])$ and $k_4 C_4([\overline{NP}], [\overline{HP}])$ describe the reaction rates for hyperphosphorylation and dephosphorylation of PER, respectively, in the reaction-limited ODE system. Thus, we can obtain the reaction probabilities for hyperphosphorylation and dephosphorylation of each individual PER molecule x with $\frac{k_2 C_2([\overline{NP}]_{x,t}, [\overline{HP}]_{x,t})}{[\overline{NP}]_{x,t}}$ and $\frac{k_4 C_4([\overline{NP}]_{x,t}, [\overline{HP}]_{x,t})}{[\overline{HP}]_{x,t}}$, where $[\overline{NP}]_{x,t}$ and $[\overline{HP}]_{x,t}$ are "local" concentrations of hypo- and hyperphosphorylated PER near the molecule x at time t:

$$[\overline{NP}]_{x,t} = \frac{1}{\Omega_L} |\{\text{Hypophosphorylated PER} \in R_t(x, 4 \cdot r_a)\}|$$
$$[\overline{HP}]_{x,t} = \frac{1}{\Omega_L} |\{\text{Hyperphosphorylated PER} \in R_t(x, 4 \cdot r_a)\}|$$

where r_a, $R_t(x, 4 \cdot r_a)$ and Ω_L denote the radius of agent, the circular local area centered at x with radius of $4 \cdot r_a$ at t and its volume, respectively. Note that $\Omega_L = 0.0064 \cdot \Omega$ where Ω is the area of the cell with radius of d; fig. S10A). As $C_2([\overline{NP}], [\overline{HP}])$ and $C_4([\overline{NP}], [\overline{HP}])$ in the Eq. 2 do not have an explicit function form, they were numerically calculated and saved. Then, they are recalled and used when the simulation is performed.

When an individual hypophosphorylated PER is hyperphosphorylated and imported to the nucleus, it is kept hyperphosphorylated, consistent with the experimental data (3, 14).

Mobility of agent

Each individual agent moves for $[t, t + \Delta t]$ as follows:

Step 1. Update the position of an individual agent.

Let $posi(t)$ be the position of an individual agent at time t. The position is changed by adding it and the movement function of the agent, $U(t)$, for each time step Δt:

$$posi(t + \Delta t) = posi(t) + U(t).$$

1) Per mRNA, nuclear PER protein and cytoplasmic obstacle were modelled to move following the two-dimensional random walk (fig. S10B (i)):

$$U(t) = \begin{cases} D_P \cdot (\cos X(t), \sin X(t)) \text{ for Per mRNA and nuclear PER protein} \\ D_o \cdot (\cos X(t), \sin X(t)) \text{ for obstacle} \end{cases}$$

where D_P and D_o denote the movement step size of *Per* mRNA and PER protein and that of an obstacle, respectively (Table 2). $X(t)$ *is* a uniform random variable on [0,2π].

2) Cytoplasmic PER protein was modelled to transit toward the perinucleus by cytoplasmic flux: it heads to the nucleus with probability p_{advec} (fig. S10B, green arrow in (ii)) and randomly moves with probability $1 - p_{advec}$ (fig. S10B, black arrow in (ii)). In other words,

$$U(t) = \begin{cases} D_P \cdot (\cos h(t), \sin h(t)) & if\ X_1(t) \le p_{advec} \\ D_P \cdot (\cos X_2(t), \sin X_2(t)) & otherwise \end{cases}$$

where $X_1(t)$and $X_2(t)$ are uniform random variables on [0,1] and on [0,2π], respectively; $h(t)$ is the polar coordinate angle of the vector heading from the position of PER protein to the center of cell. When the flux is disrupted by the obstacles, PER protein randomly moves with

$$U(t) = \frac{D_P}{2} \cdot (\cos X(t), \sin X(t))$$

(fig. S10B, red arrow in (ii)). We assumed that the movement of *Per* mRNA is not affected by the obstacles to purely focus on the movement of PER protein.

Step 2. After the position update, calculate the distance of the agent from the center of the cell, $d(t + \Delta t)$*, and the angle between the location and direction vectors of the agent,* $\theta(t + \Delta t)$ *(see fig. S10C-F).*

Step 3. If the agent overlaps with the cell membrane, adjust its position to keep it in the cytoplasm. Specifically, if $|d(t + \Delta t) - r_c| < r_a$ where r_c and r_a denote the radius of cell and that of agent, respectively, $posi(t + \Delta t)$ is adjusted to the new position inside the cytoplasmic membrane (fig. S10C).

Step 4. If the agent overlaps with the nuclear membrane, adjust its position as follows.

1) If *Per* mRNA, hypophosphorylated PER and obstacle overlap with the nuclear membrane (i.e. $|d(t + \Delta t) - r_n| < r_a$), $posi(t + \Delta t)$ is adjusted to the outside of the nuclear membrane (fig. S10D) except for when *Per* mRNA first exists the nucleus.

2) If hyperphosphorylated PER overlaps with the nuclear membrane (i.e. $|d(t + \Delta t) - r_n| < r_a$) and heads to the nucleus (i.e. $|Mod(2\pi - \theta(t + \Delta t), 2\pi) - \pi| < \frac{\pi}{2}$), it is imported to the nucleus with a probability of p_{im} (fig. S10E).

3) If hyperphosphorylated PER overlaps with the nuclear membrane (i.e. $|d(t + \Delta t) - r_n| < r_a$) and heads to the cytoplasm (i.e. $|Mod(2\pi - \theta(t + \Delta t), 2\pi) - \pi| \ge \frac{\pi}{2}$), $posi(t + \Delta t)$ is adjusted to the inside of nucleus (fig S10F).

By repeating this scheme for all agents, their position is kept updated.

Quantitative understanding for PER trafficking is far from complete. For instance, the trafficking speed of PER mRNA has not been reported. Even the measured trafficking speed of PER protein differs more than ~100-fold across studies (39, 40). Thus, for simplicity, we assumed that *Per* mRNA and PER protein have the same movement speed, D_P, and the values of D_P and p_{advec} (Table 2) were set to make the model simulate rhythmic PER expression (Fig. 3E). Note that the simulation results are robust to the choice of these values. For instance, the perturbation of D_P by 50% leads to the perturbation of period by only ~8%. The value of D_o was set to be

smaller than that of D_P (Table 2) as the obstacle is a heavy macromolecule, which is expected to move slowly.

Time-scale in the model

The model, which is considered to a normal cell (Fig. 3D and E), simulated one cycle of PER rhythm for $3794 \cdot \Delta t$ on average. Based on this, we defined $3794 \cdot \Delta t$ as 24 hr (i.e. $\Delta t = 0.006$ hr) and used the definition to calculate the simulation time in Fig 3E, G and H and Fig 4I and Fig S7.

Statistics

In this study, asterisks indicate significant p-values as follows: *, $p<0.05$; **, $p<0.01$; ***, $p<0.001$. Data across multiple experiments are shown as mean±SEM. Student's t-test was used in Fig. 1D and E. Two-way ANOVA and Bonferroni post-hoc tests were used for Fig. 1A. One-way ANOVA and Bonferroni post-hoc tests were used in Fig. 1B, fig. S1 and Fig. 3J. Leven's test was used in Fig. 5D to compare the variances of period between two groups. JTK_CYCLE (41) was used in Fig. 5F to assess the rhythmicity. Note that if the estimated p-value by JTK_CYCLE is less than 0.05, the signal was deemed to be rhythmic.

Table 1. Model rules.

No.	Rule definition
1	An individual *Per* mRNA is produced in the nucleus with a probability of p_{a_1} for each time step
2	An individual *Per* mRNA is translated with a probability of p_{a_2} for each time step when it reaches the outer periphery of the cytoplasm.
3	An individual *Per* mRNA is degraded with a probability of p_{d_1} for each time step.
4	An individual hypophosphorylated PER is hyperphosphorylated with a probability of p_{HP} for each time step.
5	An individual hypophosphorylated PER is degraded with a probability of p_{d_2} for each time step.
6	An individual hyperphosphorylated PER is dephosphorylated with a probability of p_{NP} for each time step
7	An individual hyperphosphorylated PER is degraded with a probability of p_{d_3} for each time step.
8	An individual agent moves following its movement scheme for each time step (see supplementary materials for details).

Table 2. Parameters of the spatial stochastic model. Here, $\Delta t = 0.006$ hr, and Ω is the area of the cell with radius of d (Fig S12A).

Parameter description	Symbol	Value
Reaction probability for ***Per*** mRNA production for Δt	p_{a_1}	0.015 $(1/\Delta t)$
Reaction probability for PER protein translation for Δt	p_{a_2}	0.005 $(1/\Delta t)$
Reaction probability for ***Per*** mRNA degradation for Δt	p_{d_1}	0.001 $(1/\Delta t)$
Reaction probability for hypophosphorylated PER degradation for Δt	p_{d_2}	0.001 $(1/\Delta t)$
Reaction probability for hyperphosphorylated PER degradation for Δt	p_{d_3}	0.002 $(1/\Delta t)$
The number of total activators in the nucleus	A_{tot}	500
Dissociation constant between hyperphosphorylated PER and activator	K_d	$4.68 \cdot 10^{-3}$ $(1/\Omega)$
Movement speed of ***Per*** mRNA and PER protein for Δt	D	$0.032d$ $(1/\Delta t)$
Movement speed of obstacle for Δt	D_{obs}	$0.008d$ $(1/\Delta t)$
Probability that PER protein transits toward the nucleus for Δt	p_{advec}	0.2 $(1/\Delta t)$
Probability that hyperphosphorylated PER in the cytoplasm is imported to the nucleus for Δt	p_{im}	0.01 $(1/\Delta t)$

Table 3. Parameters of the ODE system describing the multisite phosphorylation mechanism (Eq. 1). In Fig 4C and D, $k_1 = k_2 = 0.0625/\Delta t$**.** Here, $\Delta t = 0.006$ hr, and Ω is the area of the cell with radius of d (Fig S12A).

Parameter description	Symbol	Value (unit)
Binding rate constant for nonphosphorylated PER to CK1ε/δ	a_1	0.0032 ($\Omega/\Delta t$)
Binding rate constant for prime-phosphorylated PER to CK1ε/δ	a_2	0.016 ($\Omega/\Delta t$)
Binding rate constant for prime-phosphorylated PER to PP1	a_3	0.016 ($\Omega/\Delta t$)
Binding rate constant for hyperphosphorylated PER to PP1	a_4	0.0256 ($\Omega/\Delta t$)
Unbinding rate constant for nonphosphorylated PER to CK1ε/δ	d_1	10 ($1/\Delta t$)
Unbinding rate constant for prime-phosphorylated PER to CK1ε/δ	d_2	5 ($1/\Delta t$)
Unbinding rate constant for prime-phosphorylated PER to PP1	d_3	0.5 ($1/\Delta t$)
Unbinding rate constant for hyperphosphorylated PER to PP1	d_4	0.5 ($1/\Delta t$)
Phosphorylation rate constant for nonphosphorylated PER	k_1	0.011 ($1/\Delta t$)
Phosphorylation rate constant for prime-phosphorylated PER	k_2	0.15 ($1/\Delta t$)
Dephosphorylation rate constant for prime-phosphorylated PER	k_3	0.1 ($1/\Delta t$)
Dephosphorylation rate constant for hyperphosphorylated PER	k_4	0.05 ($1/\Delta t$)
Total CK1ε/δ concentration	$CK1_{tot}$	31250 ($1/\Omega$)
Total PP1 concentration	$PP1_{tot}$	7812.5 ($1/\Omega$)

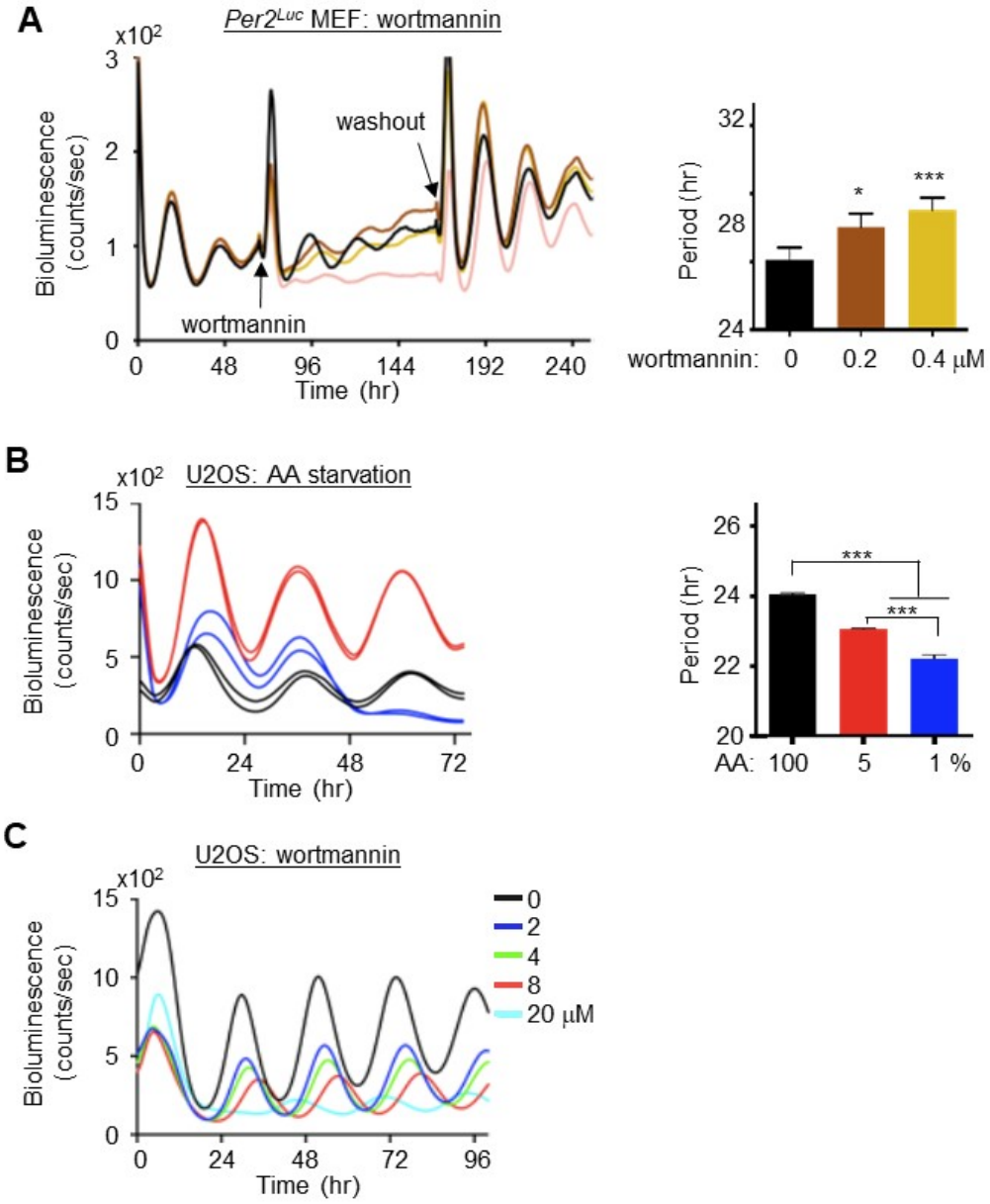

Fig. S1. Modulation of circadian rhythms by different autophagy conditions is conserved in both MEF and U2OS cells. **(A)** Circadian rhythms were lengthened by treatment of an autophagy inhibitor, wortmannin, in MEFs. N=3 each. Representative of two experiments. **(B)** Circadian rhythms were shortened by starvation in a dose-dependent manner in U2OS cells. N=3 each. Representative of two experiments. **(C)** Circadian rhythms were lengthened by wortmannin treatment in a dose-dependent manner in U2OS cells. Wortmannin samples included one sample per concentration. The results are representative of 3 experiments.

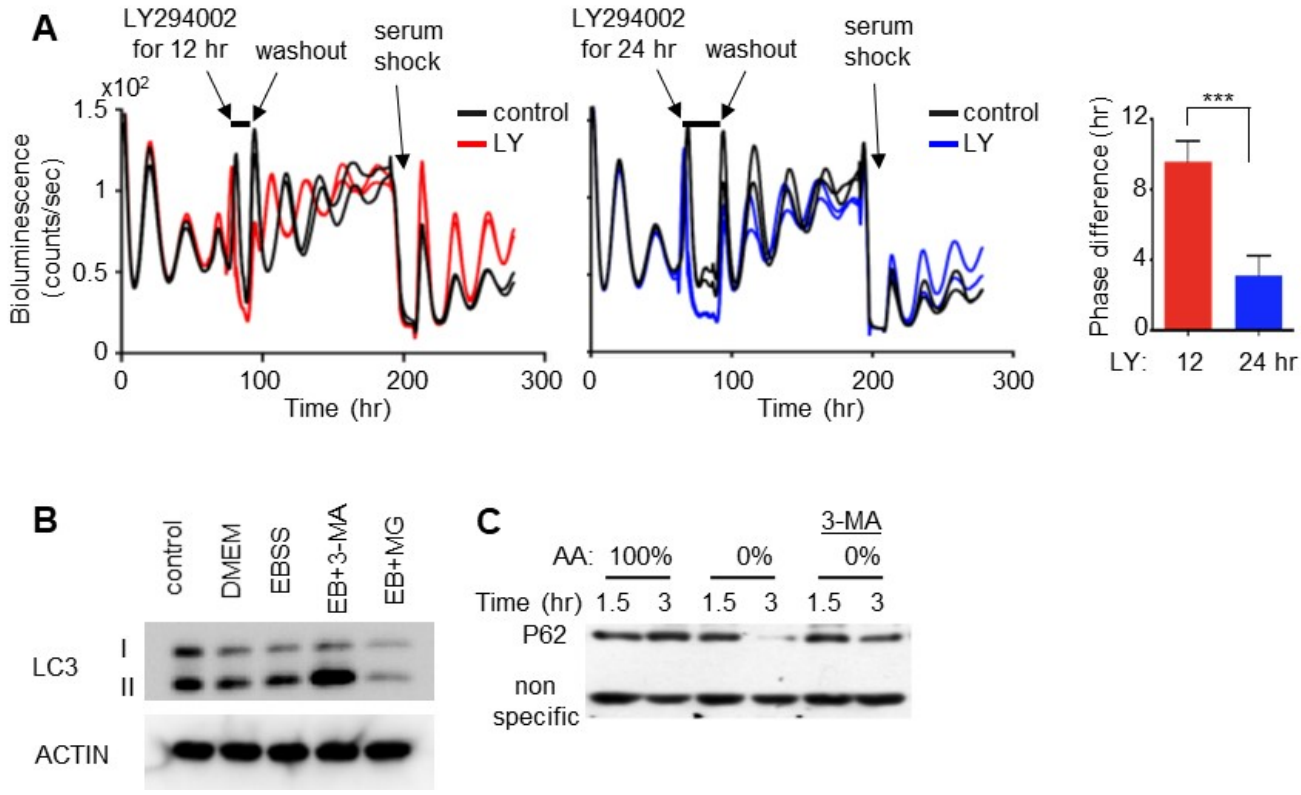

471

472

473 **Fig. S2. Disruption of circadian rhythms by autophagy inhibitors are specific to the**
474 **circadian clock. (A)** Treatment with autophagy inhibitor LY294002 produced phase-specific
475 effects. When *Per2*^{Luc} MEFs were treated with the drug for 12 hr (left) and 24 hr (middle) starting
476 3 days after the initial serum shock, the phase of the bioluminescence rhythm was dramatically
477 different after the washout while the 2nd serum shock produced the same phase regardless of
478 previous phase. N=3 each. Representative of two experiments. **(B)** 3-MA treatment for 2 hr
479 induced strong accumulation of LC-II indicating that autophagic flux was disrupted while MG132
480 treatment did not induce accumulation of the autophagy flux indicator. Representative of two
481 experiments. **(C)** 3-MA treatment inhibited degradation of P62, which is a target of active
482 autophagy. Representative of two experiments.
483

484

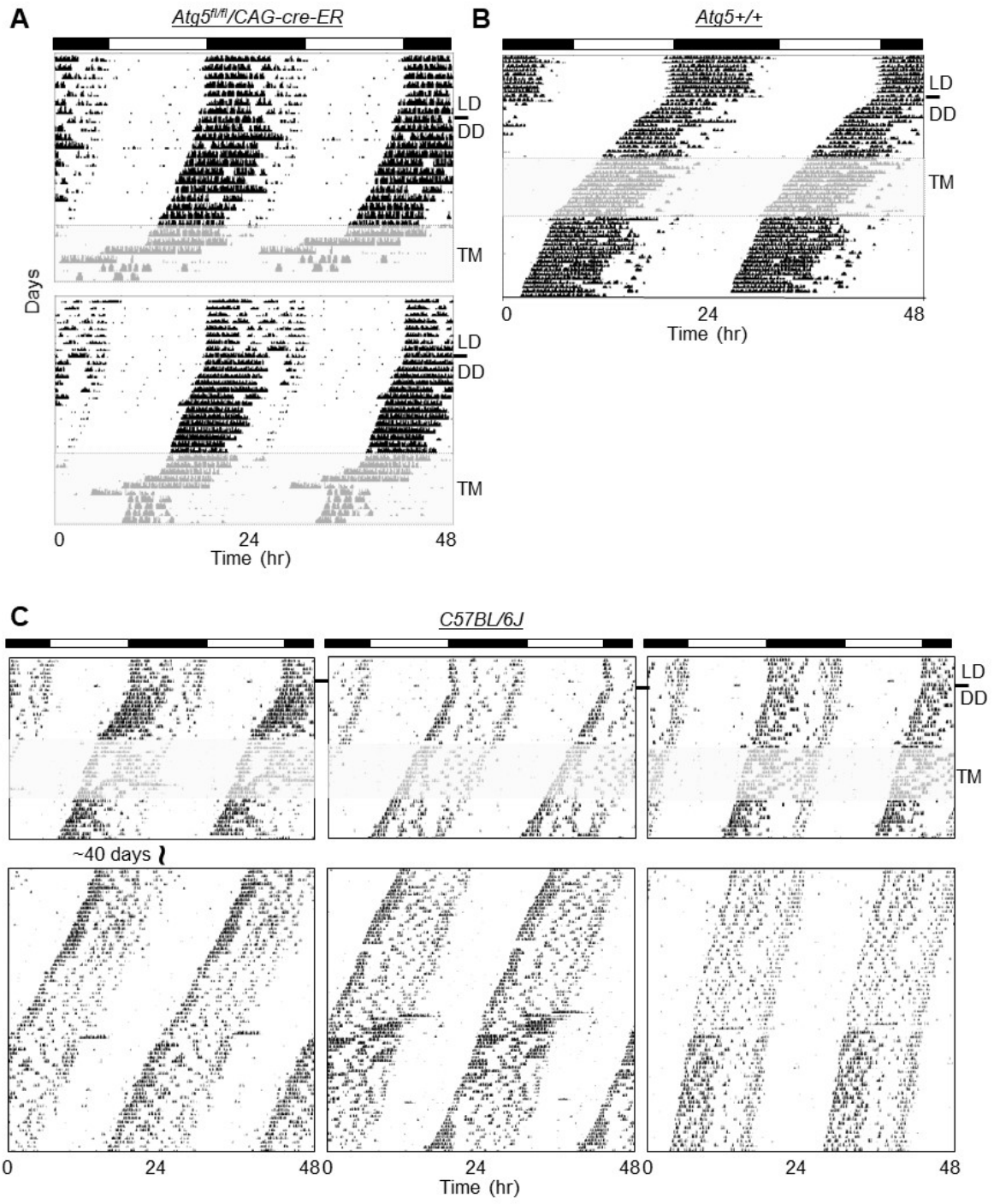

Fig. S3. Tamoxifen itself does not produce a circadian phenotype. (A) *Atg5$^{fl/fl}$; CAG-cre-ER* mutant mice died before the end of 2 weeks after treatment with TM to induce *Atg5* deletion, **(B)** while wt mice did not show any health issues or circadian phenotype from TM treatment. **(C)** After initial TM treatment in C57BL/6J mice, behavioral rhythms were measured again ~40 days later to demonstrate that TM treatment does not produce a circadian effect in the long term.

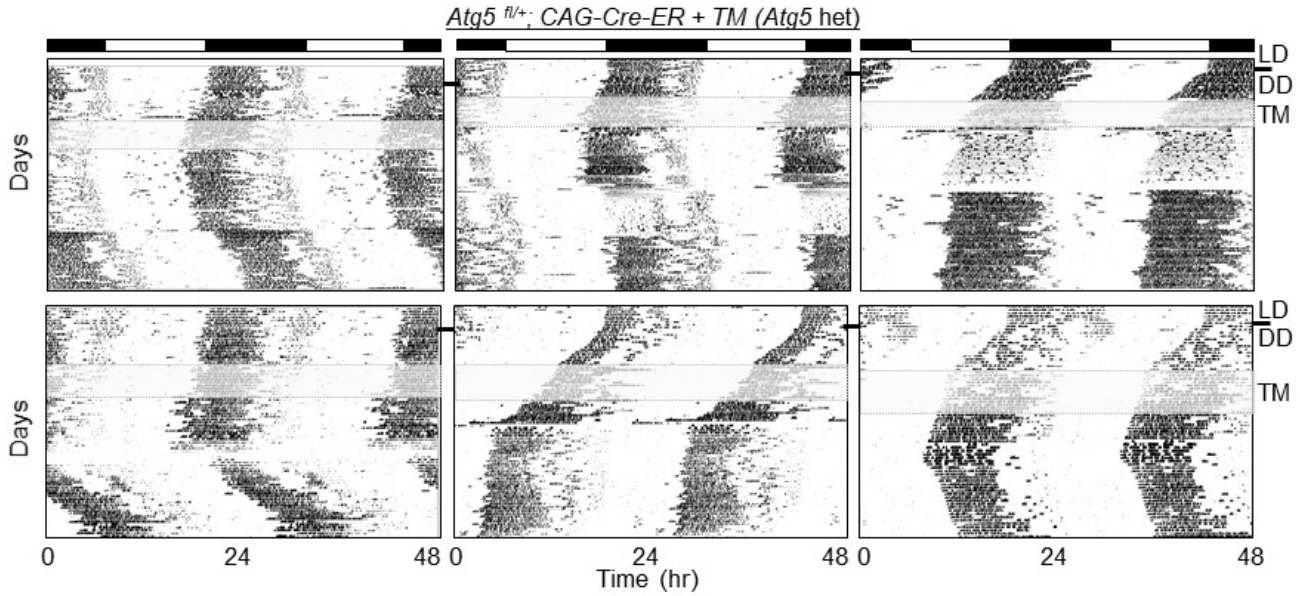

Fig. S4. No two mice show similar wake-sleep cycles. Six more *Atg5* heterozygotes are shown. Note that circadian rhythms are very irregular and noisy but generally lengthened.

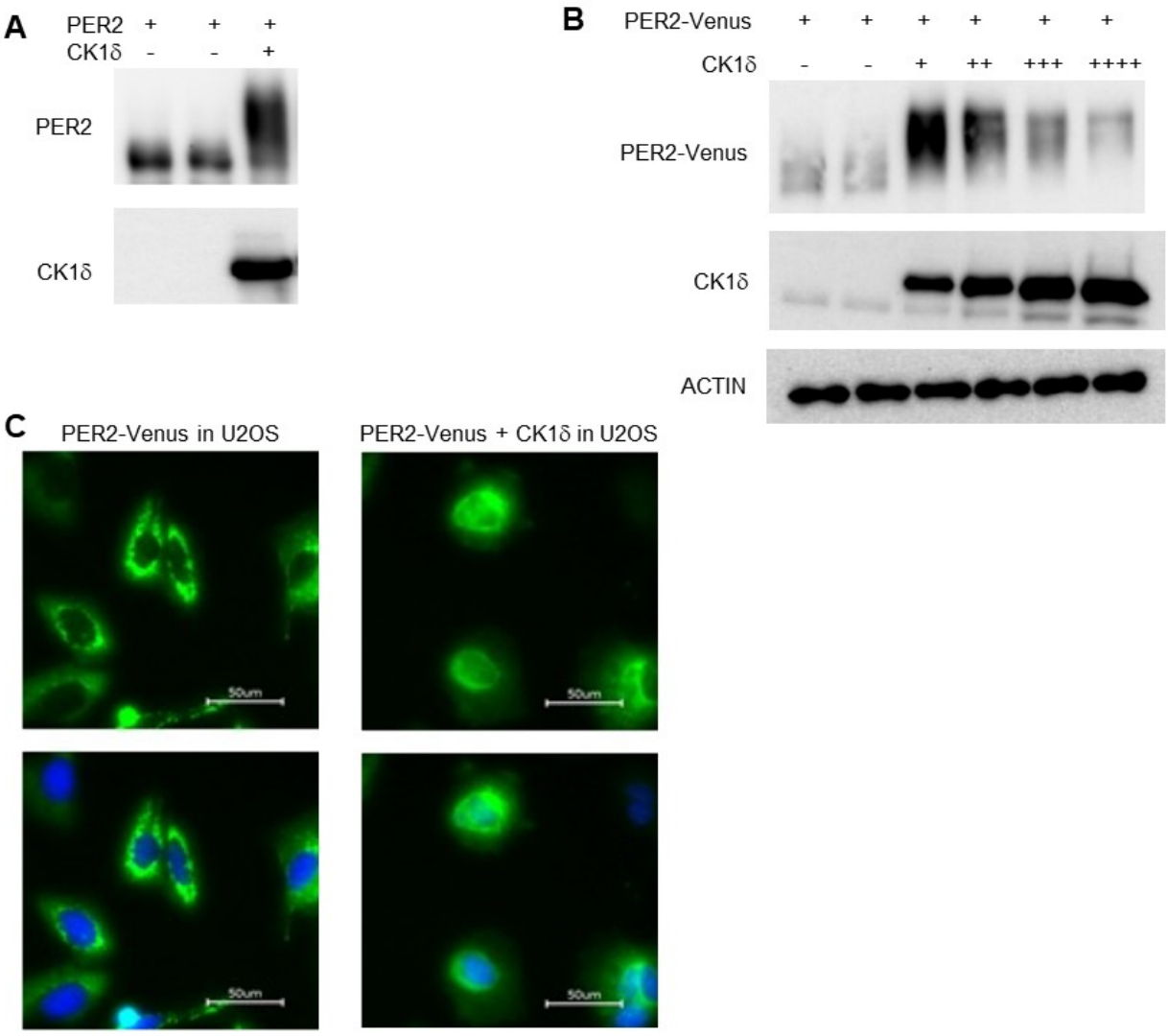

497

498 **Fig. S5. PER2-Venus is regulated by CK1δ in the same manner as PER2. (A)** PER2 is
499 robustly phosphorylated by CK1δ, when co-transfected into 293 cells. **(B)** PER2-Venus is
500 phosphorylated by CK1δ as well, and its phosphorylation and stability were CK1δ dose-
501 dependent. **(C)** Nuclear accumulation of PER2-Venus depends on CK1δ. *Per2-Venus* and *CK1δ*
502 transgenes were co-transfected into U2OS. As in Fig 2H-J, overexpressed PER2-Venus was
503 predominantly cytoplasmic but becomes nuclear if enough CK1δ was provided because CK1δ/ε
504 are limiting (3). Scale bar = 50 μm.
505

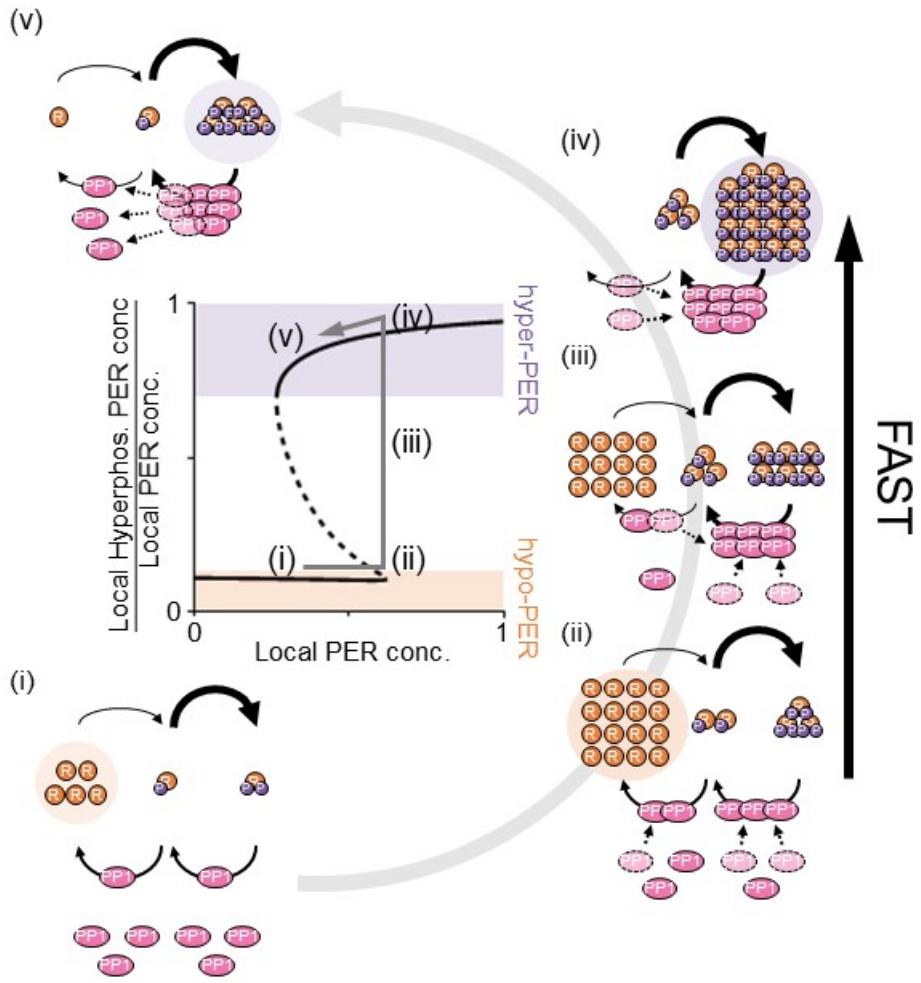

Fig. S6. Strong cooperativity in the multisite phosphorylation leads to the bistability in PER hyperphosphorylation. (i) When "local" concentration of PER is low, the majority of PER is not hyperphosphorylated because PER that is slowly phosphorylated in the priming process (thin arrow, hypophosphorylated) is rapidly dephosphorylated by PP1. The faint background circle indicates a dominant state of PER. (ii) As concentration of PER increases, the levels of prime-phosphorylated PER increase, which allows the prime-phosphorylated PER to be rapidly hyperphosphorylated (thick arrow) due to cooperativity (Fig. 3B). The more PER (as PER:CK1) is enriched in the perinucleus and hyperphosphorylated, less PP1 is available to the prime-phosphorylated PER, resulting in more hyperphosphorylated PER and thus more sequestration of PP1 by the hyperphosphorylated PER. Note that the dominant sequestration of PP1 by the hyperphosphorylated PER is mainly caused by the stoichiometric difference between hypo- and hyper-phosphorylated PER species, not by a difference in their reaction kinetic parameters as the catalytic efficiency of PP1 for hypophosphorylated PER is the nearly same as that for hyperphosphorylated PER (Table 3) (iii, iv) This positive feedback leads to the sharp increase of the hyperphosphorylated PER. (v) The high fraction of hyperphosphorylated PER persists even after PER concentration decreases. When the hyperphosphorylated PER is dephosphorylated to the prime-phosphorylated PER, the prime-phosphorylated PER is re-hyperphosphorylated rapidly (thick arrow) due to the cooperativity (Fig. 3B) and the sequestration of PP1 by hyperphosphorylated PER. Such bistability can be augmented or alternatively generated by increasing the ratio of CK1δ/ε to PP1 in the perinucleus due to stable interaction between CK1δ/ε and PER and homo- and heterodimerization of PER (42-44).

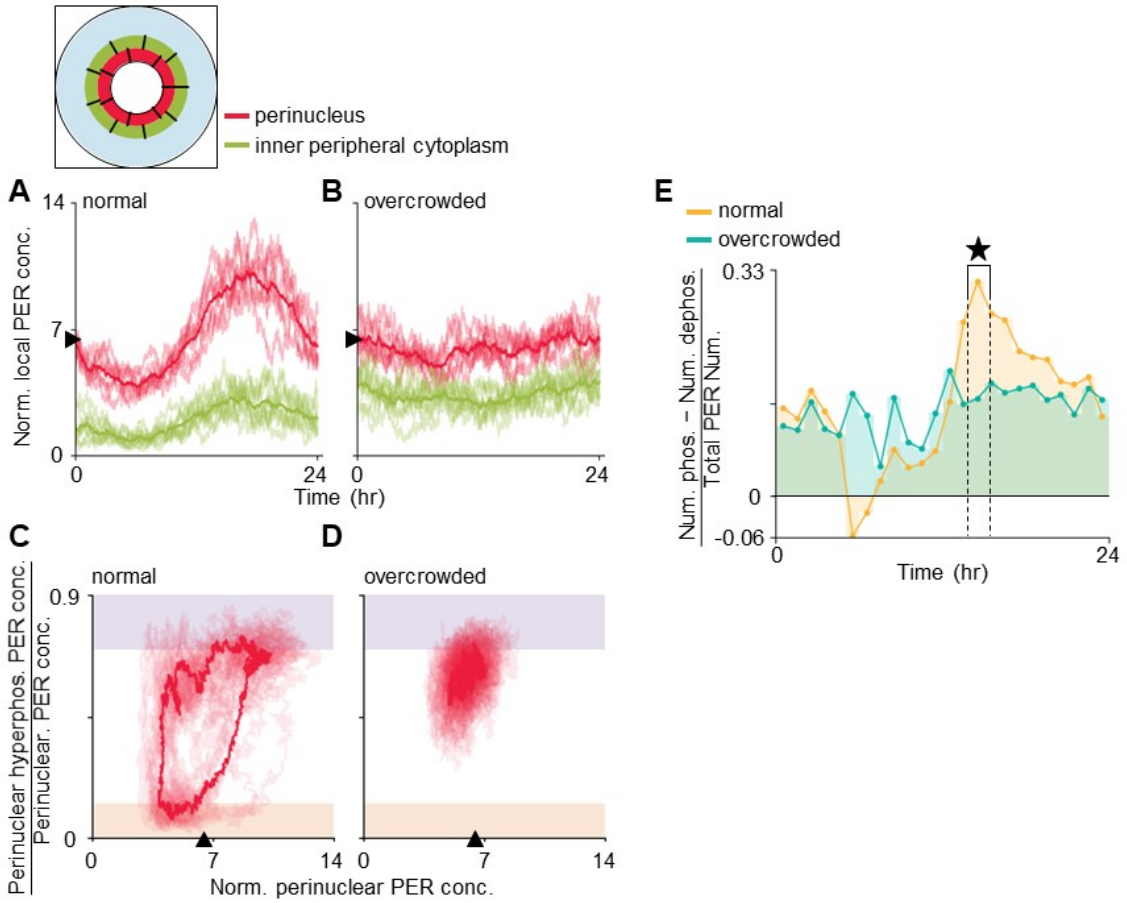

Fig. S7. The bistability is disabled in overcrowded cells. (A-D) The simulated trajectories of local PER concentration in the perinucleus and the peripheral cytoplasm (A, B) and fraction change of hyperphosphorylated PER in the local area of the perinucleus (C, D). The perinucleus (red region) and the inner peripheral cytoplasm (green region) were divided into 7 and 9 local regions, respectively. Local PER concentration (A-B) and the fraction change of hyperphosphorylated PER (C-D) were calculated from these regions, and their averages were denoted as the solid line. As the number of obstacles increases, the cytoplasmic flux (Fig. 3A (i)) is disrupted and more PER molecules are trapped in the peripheral cyotplasm (A and B; green lines and Fig. 3D and F). The peripheral cytoplasm with high levels of PER provides the perinucleus with hypophosphorylated PER over a longer period (a mild case) or constitutively (a severe case), which maintains the level of perinuclear PER around the bistability threshold (A and B; black traiangle). As a result, hyperphosphorylation and nuclear entry occur in a low amplitude and noisy manner (D). PER concentration is normalized by the peak level of total PER in a normal cell as done in Fig. 3C. **(E)** Temporal difference between phosphorylation and dephosphorylation reaction of PER, which is represented by the average total PER concentration for each 1hr bin. With normal cytoplasmic flux, dominant phosphorylation occurs at a specific circadian phase (black star), which leads to the sharp increase of the abundance of hyperphosphrylated PER (Fig. 3E, (ii)). On the other hand, this temporal regulation of phosphorylation is lost in an overcrowded cell, which disables the switch-like phosphorylation (Fig. 3G, (ii)).

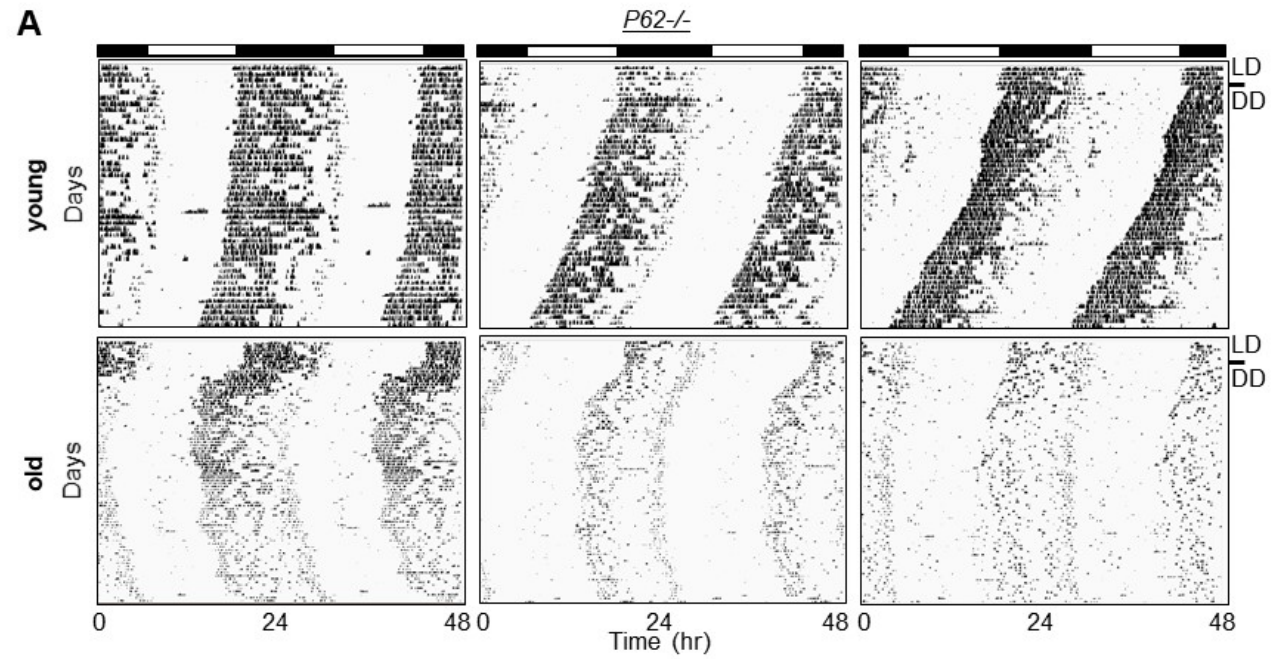

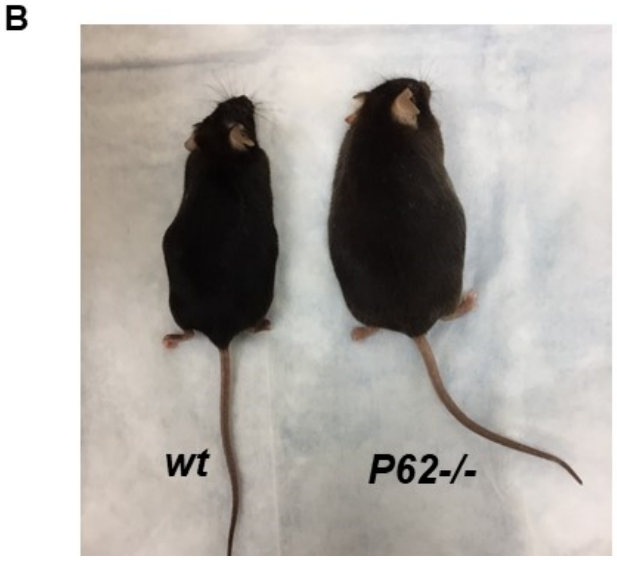

Fig. S8. Worsening of circadian disruption is associated with aging in *P62* mutant mice. **(A)** *P62* homozygous mutant mice exhibit worsening behavioral rhythms with aging. Top actograms were measured when the mice were ~3 months old while the bottom matching actograms were measured when the same mice were about 8 months old. The actograms in Fig 3I are shown when the mutant mice exhibited unstable rhythms. **(B)** All of the *P62* mutant mice became pronouncedly obese when they were ~10 months old. Age-matched 1-year old wt and *P62* mutant mice are shown.

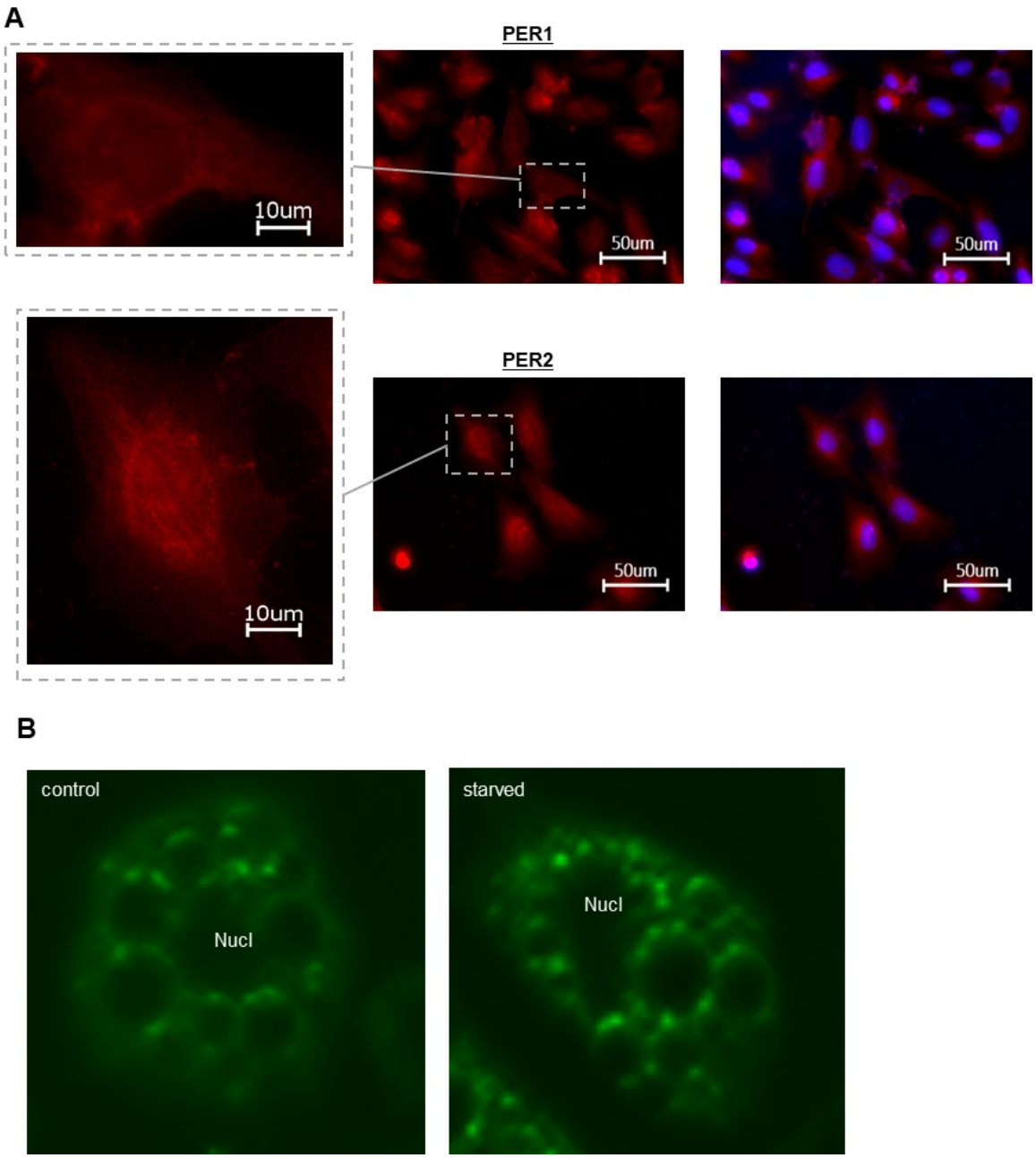

Fig. S9. Spatial regulation of PER is critical for temporal manifestation of PER rhythms. **(A)** Perinuclear ring is observed with endogenous PER1 and PER2. U2OS cells were serum-shocked and fixed 36 hours later to capture when PER levels are at their peak, to observe nuclear entry of cytoplasmic PER and PER2. Perinuclear rings were observed only in several cells per field because rings would not be as prominent as those in transgenic PER2-Venus-expressing cells. Representative single cell images are also shown. **(B)** PER2-Venus is constitutively predominantly cytoplasmic in adipocytes. The inducible adenoviral vector expressing PER2-Venus was introduced into adipocytes. Consistent with the model simulation (Fig. 3F), PER2-Venus strongly accumulated in peripheral cytoplasm as well as perinucleus even under starvation conditions (5% AA).

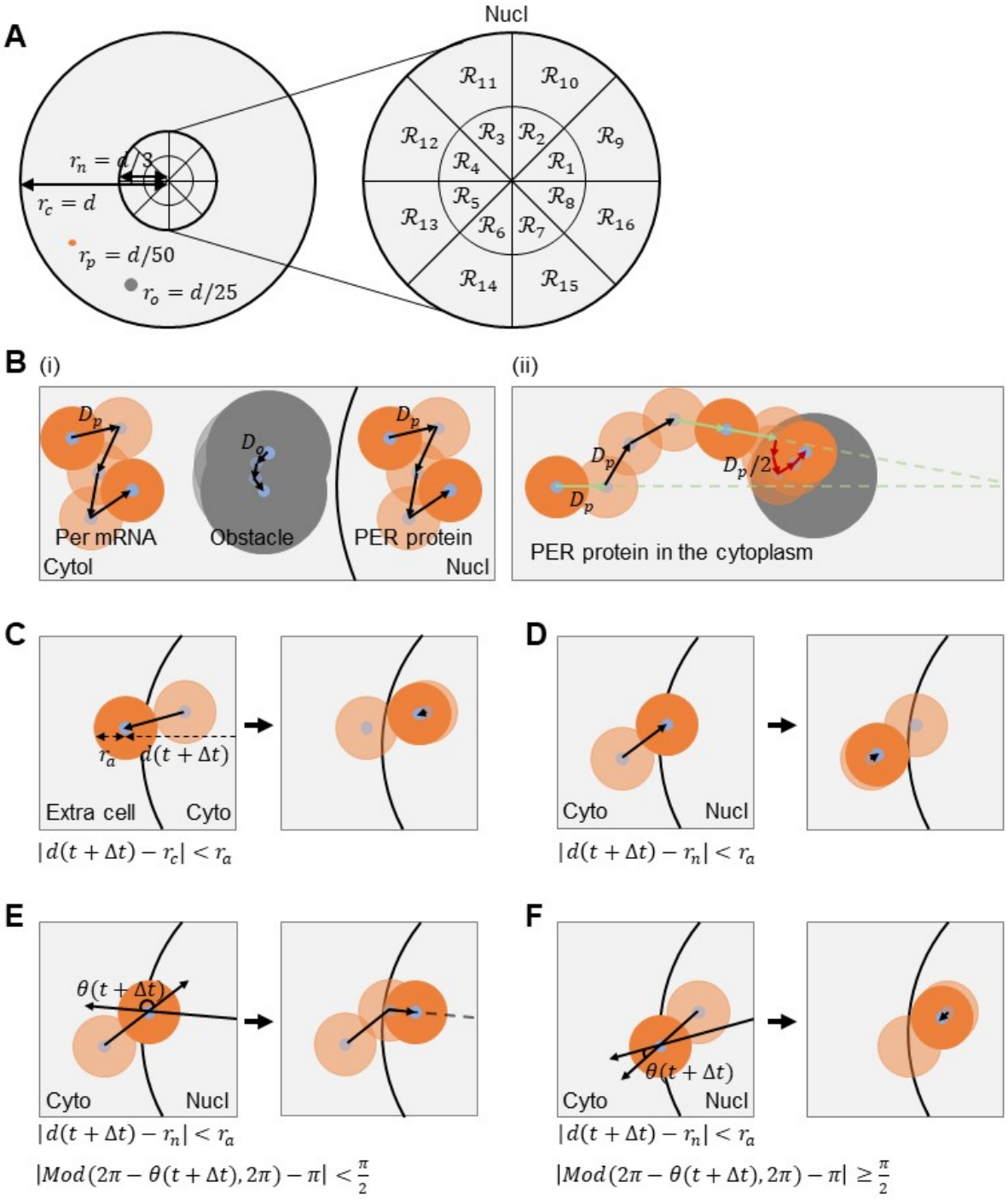

Fig. S10. Description of model components and agent mobility. (A) Shape and size of cell, nucleus, cytoplasmic obstacle, and PER molecules in the model. Their shape was defined as a circle. Their sizes were defined relative to the cell size. Specifically, relative to the cell radius ($r_c = d$), the radius of the nucleus (r_n), that of cytoplasmic obstacles (r_o), and that of PER molecules (r_p) were set to $d/3$, $d/25$ and $d/50$, respectively. The nucleus was divided into sixteen regions ($\mathcal{R}_i$ for $i = 1, \ldots, 16$) to simulate *Per* mRNA transcription (see supplementary materials for details). **(B)** (i) PER protein and cytoplasmic obstacles randomly move at each time step Δt with step size D_p and D_o, respectively (see the methods). (ii) Cytoplasmic PER protein transits toward the perinucleus by the cytoplasmic flux: it heads to the nucleus with probability p_{advec} (green arrow) and randomly moves with probability $1 - p_{advec}$ (black arrow). If PER protein is located in the region where the cytoplasmic flux is disrupted by the obstacles (gray

circle), its speed decreased by $D_p/2$ for Δt (red arrow). **(C-F)** The boundary condition of the model. The diameter of agents, i.e., obstacles or PER molecules, ($r_a = r_o$ or r_p) is set to be larger than their movement step size for Δt ($r_p > D_p$ and $r_o > D_o, see\ the\ methods$). Thus, when the agent moves to the other compartments (extracellular space, cytoplasm or nucleus), it always overlaps with the boundary (cytoplasmic or nuclear membrane) (i.e., $|d(t+\Delta t) - r_c| < r_a$ or $|d(t+\Delta t) - r_n| < r_a$ where $d(t+\Delta t)$ is the distance from the center of the cell to the position of agent at $t+\Delta t$). When the agent overlaps with the boundary, the location of the agent was adjusted according to the following rules. 1) Agent cannot be exported out of the extracellular space. If the agent overlaps with the cytoplasmic membrane ($|d(t+\Delta t) - r_c| < r_a$), its position is adjusted back to the position where it collided with the cytoplasmic membrane (C). 2) *Per* mRNA and hypophosphorylated PER cannot be imported into the nucleus: if they overlap with the nuclear membrane ($|d(t+\Delta t) - r_n| < r_a$), their position is adjusted back to the position where they collided with the nuclear membrane (D). 3) Hyperphosphorylated PER is imported to the nucleus with a probability of p_{im} for Δt. If hyperphosphorylated PER overlaps with the nuclear membrane ($|d(t+\Delta t) - r_n| < r_a$) and heads to the nucleus ($|Mod(2\pi - \theta(t+\Delta t), 2\pi) - \pi| < \frac{\pi}{2}$), it further moves toward the center of the cell with a probability of p_{im} until it touches the nuclear membrane inside the nucleus (E). 4) Hyperphosphorylated PER cannot be exported from the nucleus to the cytoplasm. If hyperphosphorylated PER overlaps with the nuclear membrane ($|d(t+\Delta t) - r_n| < r_a$) and heads to the cytoplasm ($|Mod(2\pi - \theta(t+\Delta t), 2\pi) - \pi| \geq \frac{\pi}{2}$), its position is adjusted back to the position where it collided with the nuclear membrane (F).

Movie S1. Real time monitoring of PER2-Venus trafficking in U2OS cells.

References

1. Chen R, D'Alessandro M, & Lee C (2013) miRNAs are required for generating a time delay critical for the circadian oscillator. *Curr Biol* 23(20):1959-1968.
2. Sundaram S*, et al.* (2019) Inhibition of casein kinase 1delta/epsilonimproves cognitive-affective behavior and reduces amyloid load in the APP-PS1 mouse model of Alzheimer's disease. *Sci Rep* 9(1):13743.
3. Lee C, Etchegaray JP, Cagampang FR, Loudon AS, & Reppert SM (2001) Posttranslational mechanisms regulate the mammalian circadian clock. *Cell* 107(7):855-867.
4. Lee C, Weaver DR, & Reppert SM (2004) Direct association between mouse PERIOD and CKIepsilon is critical for a functioning circadian clock. *Mol Cell Biol* 24(2):584-594.
5. Jin YH*, et al.* (2019) Streamlined procedure for gene knockouts using all-in-one adenoviral CRISPR-Cas9. *Sci Rep* 9(1):277.
6. D'Alessandro M*, et al.* (2015) A tunable artificial circadian clock in clock-defective mice. *Nat Commun* 6:8587.
7. He TC*, et al.* (1998) A simplified system for generating recombinant adenoviruses. *Proc Natl Acad Sci U S A* 95(5):2509-2514.

8. Chen R, *et al.* (2009) Rhythmic PER abundance defines a critical nodal point for negative feedback within the circadian clock mechanism. *Mol Cell* 36(3):417-430.
9. Stevanovic K, *et al.* (2017) Disruption of normal circadian clock function in a mouse model of tauopathy. *Exp Neurol* 294:58-67.
10. Kim JK & Forger DB (2012) A mechanism for robust circadian timekeeping via stoichiometric balance. *Mol Syst Biol* 8:630.
11. Kim JK, Kilpatrick ZP, Bennett MR, & Josic K (2014) Molecular mechanisms that regulate the coupled period of the mammalian circadian clock. *Biophys J* 106(9):2071-2081.
12. Kim JK, Josic K, & Bennett MR (2015) The relationship between stochastic and deterministic quasi-steady state approximations. *Bmc Syst Biol* 9.
13. Kim JK (2016) Protein sequestration versus Hill-type repression in circadian clock models. *IET Syst Biol* 10(4):125-135.
14. D'Alessandro M, *et al.* (2017) Stability of Wake-Sleep Cycles Requires Robust Degradation of the PERIOD Protein. *Curr Biol* 27(22):3454-3467 e3458.
15. Bonabeau E (2002) Agent-based modeling: methods and techniques for simulating human systems. *Proceedings of the National Academy of Sciences of the United States of America* 99 Suppl 3:7280-7287.
16. Sklar E (2007) NetLogo, a multi-agent simulation environment. *Artif Life* 13(3):303-311.
17. Alberts B (2008) *Molecular biology of the cell* (Garland Science, New York) 5th Ed.
18. Banisch S & Lima R (2015) Markov Chain Aggregation for Simple Agent-Based Models on Symmetric Networks: The Voter Model. *Adv Complex Syst* 18(3-4).
19. Gillespie DT (2001) Approximate accelerated stochastic simulation of chemically reacting systems. *J Chem Phys* 115(4):1716-1733.
20. Gardiner CW (2009) *Stochastic methods : a handbook for the natural and social sciences* (Springer, Berlin) 4th Ed pp xvii, 447 p.
21. Gillespie DT (1976) General Method for Numerically Simulating Stochastic Time Evolution of Coupled Chemical-Reactions. *J Comput Phys* 22(4):403-434.
22. Kampen NGv (2007) *Stochastic processes in physics and chemistry* (Elsevier, Amsterdam ; Boston) 3rd Ed pp xvi, 463 p.
23. El Samad H, Khammash M, Petzold L, & Gillespie D (2005) Stochastic modelling of gene regulatory networks. *Int J Robust Nonlin* 15(15):691-711.
24. Frazier Z & Alber F (2012) A Computational Approach to Increase Time Scales in Brownian Dynamics-Based Reaction-Diffusion Modeling. *J Comput Biol* 19(6):606-618.
25. Vanselow K, *et al.* (2006) Differential effects of PER2 phosphorylation: molecular basis for the human familial advanced sleep phase syndrome (FASPS). *Genes Dev* 20(19):2660-2672.
26. Zhou M, Kim JK, Eng GWL, Forger DB, & Virshup DM (2015) A Period2 phosphoswitch regulates and temperature compensates circadian period. *Molecular cell* 60(1):77-88.
27. Vanselow K & Kramer A (2007) Role of phosphorylation in the mammalian circadian clock. *Cold Spring Harbor symposia on quantitative biology*, (Cold Spring Harbor Laboratory Press), pp 167-176.
28. Tzafriri AR (2003) Michaelis-Menten kinetics at high enzyme concentrations. *B Math Biol* 65(6):1111-1129.
29. Kumar A & Josic K (2011) Reduced models of networks of coupled enzymatic reactions. *Journal of theoretical biology* 278(1):87-106.
30. Barik D, Paul MR, Baumann WT, Cao Y, & Tyson JJ (2008) Stochastic simulation of enzyme-catalyzed reactions with disparate timescales. *Biophysical Journal* 95(8):3563-3574.

31. MacNamara S, Bersani AM, Burrage K, & Sidje RB (2008) Stochastic chemical kinetics and the total quasi-steady-state assumption: Application to the stochastic simulation algorithm and chemical master equation. *J Chem Phys* 129(9).
32. Kim JK, Josic K, & Bennett MR (2014) The Validity of Quasi-Steady-State Approximations in Discrete Stochastic Simulations. *Biophysical Journal* 107(3):783-793.
33. Soh S, Byrska M, Kandere-Grzybowska K, & Grzybowski BA (2010) Reaction-Diffusion Systems in Intracellular Molecular Transport and Control. *Angew Chem Int Edit* 49(25):4170-4198.
34. Sturrock M, Terry AJ, Xirodimas DP, Thompson AM, & Chaplain MAJ (2011) Spatio-temporal modelling of the Hes1 and p53-Mdm2 intracellular signalling pathways. *Journal of theoretical biology* 273(1):15-31.
35. Sturrock M, Terry AJ, Xirodimas DP, Thompson AM, & Chaplain MAJ (2012) Influence of the Nuclear Membrane, Active Transport, and Cell Shape on the Hes1 and p53-Mdm2 Pathways: Insights from Spatio-temporal Modelling. *B Math Biol* 74(7):1531-1579.
36. D'Onofrio A, Cerrai P, & Gandolfi A (2012) *New challenges for cancer systems biomedicine* (Springer Verlag, Milan ; New York) pp xi, 398 p.
37. Shibata Y, Voeltz GK, & Rapoport TA (2006) Rough sheets and smooth tubules. *Cell* 126(3):435-439.
38. Narasimamurthy R*, et al.* (2018) CK1delta/epsilon protein kinase primes the PER2 circadian phosphoswitch. *Proceedings of the National Academy of Sciences of the United States of America* 115(23):5986-5991.
39. Ollinger R*, et al.* (2014) Dynamics of the circadian clock protein PERIOD2 in living cells. *J Cell Sci* 127(Pt 19):4322-4328.
40. Smyllie NJ*, et al.* (2016) Visualizing and Quantifying Intracellular Behavior and Abundance of the Core Circadian Clock Protein PERIOD2. *Curr Biol* 26(14):1880-1886.
41. Hughes ME, Hogenesch JB, & Kornacker K (2010) JTK_CYCLE: an efficient nonparametric algorithm for detecting rhythmic components in genome-scale data sets. *Journal of biological rhythms* 25(5):372-380.
42. Rombouts J, Vandervelde A, & Gelens L (2018) Delay models for the early embryonic cell cycle oscillator. *PLoS One* 13(3):e0194769.
43. Gelens L, Qian J, Bollen M, & Saurin AT (2018) The Importance of Kinase-Phosphatase Integration: Lessons from Mitosis. *Trends Cell Biol* 28(1):6-21.
44. Ferrell JE, Jr., Tsai TY, & Yang Q (2011) Modeling the cell cycle: why do certain circuits oscillate? *Cell* 144(6):874-885.